Structural and Morphological Description of Sn/SnO x Core–Shell Nanoparticles Synthesized and Isolated from Ionic Liquid

Nadia Soulmi, Damien Dambournet, Cécile Rizzi, Juliette Sirieix-Plénet, Mathieu Duttine, Alain Wattiaux, Jolanta Swiatowska, Olaf J. Borkiewicz, Henri Groult, Laurent Gaillon

Structural and morphological description of Sn/SnO_x core-shell nanoparticles synthesized and isolated from ionic liquid

Nadia Soulmi [a,], Damien Dambournet [a], Cécile Rizzi [a], Juliette Sirieix-Plénet [a], Mathieu Duttine [b], Alain Wattiaux [b], Jolanta Swiatowska [c], Olaf J. Borkiewicz [d], Henri Groult [a], and Laurent Gaillon [a,*]*

[a] Sorbonne Universités, UPMC Univ Paris 06, CNRS, Laboratoire PHENIX, F-75005 Paris, France

[b] CNRS, Université de Bordeaux, ICMCB, UPR 9048, F-33600 Pessac, France

[c] PSL Research University, Chimie ParisTech - CNRS, Institut de Recherche de Chimie Paris, F-75005 Paris, France

[d] X-ray Science Division, Advanced Photon Source, Argonne National Laboratory, Argonne, Illinois 60439, United States

KEYWORDS. Room temperature ionic liquids, Core-shell nanoparticles, Washing, Mössbauer spectroscopy, Pair Distribution Function.

ABSTRACT.

The potential application of high capacity Sn-based electrode materials for energy storage, particularly in rechargeable batteries, has led to extensive research activities. In this scope, the development of innovative synthesis route allowing to downsize particles to the nanoscale is of particular interest owing to the ability of such nanomaterial to better accommodate volume changes upon electrochemical reactions. Here, we report on the use of room temperature ionic liquid (*i.e.* $[EMIm^+][TFSI^-]$) as solvent, template and stabilizer for Sn-based nanoparticles. In such a media, we observed, using Cryo-TEM, that pure Sn nanoparticles can be stabilized. Further washing steps are, however, mandatory to remove residual ionic liquid. It is shown that the washing steps are accompanied by the partial oxidation of the surface leading to core-shell structured Sn/SnO_x composite. To understand the structural features of such a complex architecture, HRTEM, Mössbauer spectroscopy and the pair distribution function were employed to reveal a crystallized β-Sn core and a SnO and SnO_2 amorphous shell. The proportion of oxidized phases increases with the final washing step with water, which appeared necessary not only to remove salts but also the final surface impurities made of the cationic moieties of the ionic liquid. This work highlights the strong oxidation reactivity of Sn-based nanoparticles, which needs to be taken into account when evaluating their electrochemical properties.

INTRODUCTION.

Sn is a metal of choice for a substantial number of studies and several applications,[1–5] including negative electrode materials for lithium-ion batteries (LIBs).[6–9] When used as material for electrode, Sn reacts with lithium to form various Li_xSn types of compounds that can provide high theoretical specific capacity of 993 $mAh.g^{-1}$ for $Li_{4.4}Sn$ (compared to 372 $mAh.g^{-1}$ for commercial graphite negative electrodes). Nevertheless, the volume changes of Sn-based electrode materials

(> 290%) associated with alloying/de-alloying processes induce high mechanical stress leading to electrode failure and cyclability issues.[10] To overcome these drawbacks, several approaches have been developed to improve their electrochemical performance, such as specific capacity, rate capability, and cycling stability. Nanostructuration is a strategy of choice to buffer the volume changes and to reach higher conductivity between the grains without loss of mechanical properties, and thus even more efficiently when it is associated with an accurate control of the electrode composition: by either (i) embedding Sn into carbon to form Sn/C based composites, (ii) searching new synthesis for Sn-based intermetallic compounds.[6–12]

In order to reduce the length of the diffusion path of the Li^+ ions within the particles,[13] the control of the particle size appears to be one of the essential parameters when developing new route of synthesis. Over the last few decades, various techniques have been developed to synthesize nanoparticles (NPs). A suitable route relies on a bottom-up chemical synthesis in soft reaction conditions operating in a liquid phase.[14–17] Typically, the reduction of metallic salts or organometallic compounds under inert atmosphere have been used, and generally stabilizing agents are added to the reaction medium to prevent aggregation and to further provide a protective layer around the NPs.[18–20] However, these methods require additional steps such as thermal decomposition or a supplemental heating step.

As an alternative to these conventional procedures, use of "innovative" solvents such as ionic liquids (IL) offer a suitable option. They are generally liquid in a wide range of temperatures, show negligible vapor pressure [21] and offer new opportunities for the synthesis of metallic NPs owing to their large thermal, chemical, and electrochemical stability.[22] They indeed behave as template and solvent, but also as stabilizers for NPs surface to prevent their aggregation. Through their structuration, they offer nanodomains that can act as "nanoreactors" or are also able to isolate

metallic NPs without requirement of any additional surface stabilizers.[23] Likewise, it is possible to control the size, the shape and the dispersion of NPs by tuning the nature of the anion or the cation, or the alkyl side chain length.[24,25]

Recently, we developed a synthesis route at room temperature for Sn-based nanomaterials using Sn salts and hydride reducing agent in IL. Smooth reaction conditions were promoted, and the role of capping agent played by the solvent itself did not require introducing any another component in the reaction mixture. We already showed the influence of water on the loss of the capping properties of the IL toward the surface of Sn during the synthesis of NPs, [26] as water content is well known to greatly affect nanostructuration and properties of IL.[27] For this reason the use of hydrophobic IL containing bis(trifluoromethanesulfonyl)imide anion ($[TFSI^-]$) is notably advantageous. Furthermore, the self-organized structure with 3D arrangement of imidazolium-based IL with polar and nonpolar nanoregions allows to form nanosized particles.[22,28] Therein, we made the choice for this study to use the 1-ethyl-3-methylimidazolium bis(trifluoromethanesulfonyl)imide $[EMIm^+][TFSI^-]$ IL, which structure is given in Figure 1, because it combines all the aforementioned criteria.

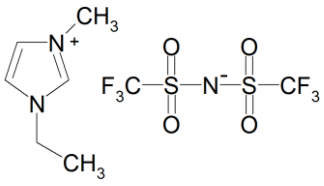

Figure 1. Chemical structure of $[EMIm^+][TFSI^-]$

Furthermore, we proved the feasibility of this approach to develop a Sn-based negative electrode material for LIB. Nevertheless owing to a non-negligible amount of IL into the electrode composite, the gravimetric capacity was dramatically affected. It is crucial, before undertaking the use of these NPs as active negative electrode material for LIB, to examine thoroughly their composition in order to improve and to understand further their electrochemical behavior. Additionally, to our knowledge, there are only few studies [29] that investigate how to isolate NPs free of IL and describe their fine structures.

In this study, we report after Sn NPs synthesis, works toward (i) isolating of Sn NPs free from IL and (ii) solving the composition, the crystallinity and the atomic structure of isolated NPs of Sn.

MATERIALS AND METHODS.

Synthesis. Anhydrous tin (II) chloride ($SnCl_2$, 99%, Alfa Aesar), anhydrous sodium borohydride ($NaBH_4$, 99.9 %, Sigma Aldrich), 1-ethyl-3-methylimidazolium bis(trifluoromethanesulfonyl)imide ($[EMIm^+][TFSI^-]$, 99.5 %, Solvionic), acetonitrile (ACN, HPLC grade, 99%, Sigma Aldrich), acetone (HPLC grade, 99%, VWR) and methanol (HPLC grade, 99%,VWR) were used as received.

The NPs were synthesized following the methodology developed in our laboratory.[26] It consists in the reduction of $SnCl_2$ (40 mM – 7.6 mg) with $NaBH_4$ (400 mM - 15.2 mg) initially separately dissolved into the IL (1 mL). The two solutions were rapidly mixed and left under stirring at room temperature during 6 hours. A black color immediately appeared after mixing, which confirmed a fast reaction. All experiments were performed in a dry glove box filled with argon.

NPs isolation. Sn NPs were isolated following several steps. First, they were centrifugated at 10000 RPM for 10 min in order to remove the IL. Then, Sn NPs were washed under controlled atmosphere of nitrogen with ACN, redispersed and stirred with a vortex (1 min) and isolated by centrifugation at 6000 RPM for 5 min, 7 times. Thirdly, Sn NPs were washed again with acetone followed by vortex stirring and centrifugation at 6000 RPM for 5 min, 3 times. Then, an ultimate washing with distilled water (1 mL) was carried out in order to remove all possible impurities. At last, NPs were dried at room temperature under nitrogen flux.

Characterization methods. Powder X-ray diffraction (PXRD) was performed using a Rigaku Ultima IV X-ray diffractometer with a Cu Kα radiation (λ= 1.54059 Å) with a scan rate of $0.1°.min^{-1}$ between 10 and 80° (2θ).

NPs were characterized by Transmission electron microscopy (TEM) using a JEOL 1011 microscope at an accelerating voltage of 100 kV. High resolution transmission electron microscopy (HRTEM) analysis were performed using a JEOL 2010 microscope operating at 200 kV (LaB_6). Samples were prepared by dispersing few mg of Sn NPs powder in methanol, 5 drops of this suspension were placed on a 200 mesh carbon coated copper grid, drying 1 minute between each drop.

Cryo-transmission electron microscopy (Cryo-TEM) was used to observe before isolation, NPs directly in IL media. Just after the synthesis, a drop of the solution was deposited on a 200 mesh holey carbon coated grid, then the excess of liquid on the grid was absorbed with a filter paper and the membrane was quench-frozen rapidly in liquid ethane. The grid was mounted and inserted in the microscope using a nitrogen cooled side entry Gatan 626 cryo-holder. Observations were carried out at low temperature (-180 °C) using a LaB_6 JEOL 2100 cryo-microscope operating at

an accelerating voltage of 200 kV and the micrographs were recorded on an ultrascan 2k CCD camera (Gatan).

Thermogravimetric analysis (TGA) were performed using a TA Instruments SDT Q600 apparatus. Samples were heated from room temperature up to 800 °C at a constant heating rate of 10 °C.min^{-1} under nitrogen atmosphere with a constant flow rate of 100 mL.min^{-1}.

^{119}Sn Mössbauer measurements were carried out using a constant-acceleration Halder-type spectrometer operating in transmission geometry with a room temperature ^{119m}Sn ($CaSnO_3$) source (370 MBq). Thin absorbers containing about 15 mg.cm^{-2} of Sn (^{119}Sn natural abundance 8.59 %) were placed into a liquid helium bath cryostat. Spectra were recorded from room temperature down to 4.2 K and the refinement of Mössbauer hyperfine parameters (δ isomer shift, Δ quadrupole splitting, Γ Lorentzian linewidth and relative areas) was performed using both homemade programs and the WinNormos® software (Wissenschaftliche Elektronik GmbH).[30] The ^{119}Sn isomer shifts are referenced to $BaSnO_3$ at room temperature.

High-energy X-ray data were collected at the 11-ID-B station at the Advanced Photon Source (Argonne National Laboratory) with an X-ray energy of 86.7 keV (λ=0.1430 Å). After corrections (background and Compton scattering), Pair Distribution Functions (PDFs), G(r) were extracted from the data using PDFgetX2 software.[31] Refinements of the PDF data were performed using PDFgui,[32] with structural models from ICSD database.[33] Refined parameters were the instrument parameters, the lattice parameters, the atomic positions, and the scale factor. The coherence length was refined using the spherical particle size parameter. All samples were packed in Kapton capillaries (Cole-Parmer®) with an epoxy resin sealing. Structural models were used to compare the correlation with the modeling PDF data, otherwise, quantitative compositional information was

obtained by the scale factors when several phases were present.[34] The difference between the experimental observation (data) and the calculated values (model) correspond to the residual curve, which compute the quality of the refinement defined by the weighted R-factor noted R_w.

The chemical composition of the surface was analyzed by X-ray photoelectron spectroscopy (XPS) with a VG Escalab 250 spectrometer with a UHV preparation chamber directly connected to the glove box. An Al Kα monochromatized radiation (hν = 1486.6 eV) was employed as X-ray source. The binding energies were calibrated versus the carbon signal at 285.0 eV. Survey spectra were recorded with a pass energy of 100 eV and high resolution spectra of the XPS C 1s and Sn 3d, valence band region were recorded with a pass energy of 20 eV.

RESULTS AND DISCUSSION.

The chemical reaction of solvated $SnCl_2$ and $NaBH_4$ in IL led to instantaneous precipitation of NPs composed of metallic Sn.[26] In such reaction process, IL acts as a solvent and a capping agent of NPs. Although, the surface functionalization of NPs by the IL allows preventing crystal growth and therefore enables to stabilize NPs in solution, its complete removal remains a key step of the synthesis.

NPs washing. In our previous study,[26] acetone was used to wash NPs. This choice was based on the procedures commonly used and reported in the literature [35] that usually employ polar and aprotic solvents. Nevertheless, as revealed by X-ray photoelectron spectroscopy (XPS), it was found that a certain amount of IL was always present at the surface of the sample, with both anionic and cationic moieties even after several washing steps. In order to improve the washing procedure, we further use ACN, in addition to acetone due to its higher polarity and its good miscibility to IL.[36]

The surface composition of the NPs washed with ACN and acetone was studied by XPS. Survey spectrum (Figure 2) showed clearly the presence of Sn (with 3 Sn peaks, Sn 3d between 484 and 502 eV, Sn 3s at 900 eV and Sn 3p between 700 and 760 eV).[37] Three peaks located at around 285, 400 and 531 eV were assigned to the C 1s, N 1s and O 1s, respectively. Cl 2p (200 eV), Cl 2s (280 eV), Na 1s (1075 eV) and B 1s (193 eV) assigned peaks were attributed to side products from precursors.

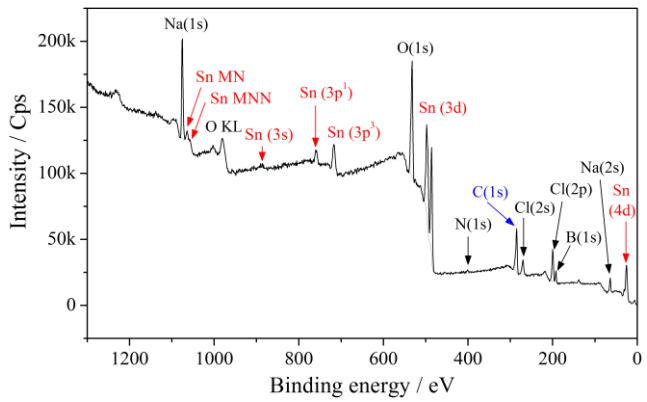

Figure 2. XPS survey spectrum of Sn NPs synthesized in [EMIm$^+$][TFSI$^-$] washed with ACN + acetone.

A decomposition of C 1s core level spectra (Figure 3.a) presents four peaks located at 285, 286.3, 288.6, and 289.8 eV and, which were assigned to C4, C3, C2, and C1, respectively, of the [EMIm$^+$] cation (see inset Figure 3.a). The presence of C-N bond (C3) peak can be also confirmed by the appearance of small intensity N1s peak at around 400 eV. Here, the peak at 292 eV attributed to the carbon of IL anion [TFSI$^-$] according to bibliographic data [38] was not present, meaning, that residues of IL present on the surface sample were only composed of the imidazolium moieties. This result highlighted the strong interaction of imidazolium cation with the surface of the NPs, in agreement with several studies demonstrating the stabilizing role of the cation of IL.[39–41] However,

it should be emphasized that these four carbon peaks assigned to the [EMIm$^+$] cation can be also superimposed with the peaks attributed to surface organic contaminations such as C-C, C-O, C=O. which could partially explain the observed lineshape.[42,43]

The Sn 3d core level spectrum displays 5/2 and 3/2 spin orbit doublet. A decomposition of the Sn $3d_{5/2}$ core level spectrum (Figure 3.b) showed three peaks at 484.6, 486.5 and 488.6 eV. The first and the second one can be attributed to the metallic Sn, and to an oxidized phase of SnO_x, respectively.[42,44] The latest peak remained undefined due to its high binding energy value.

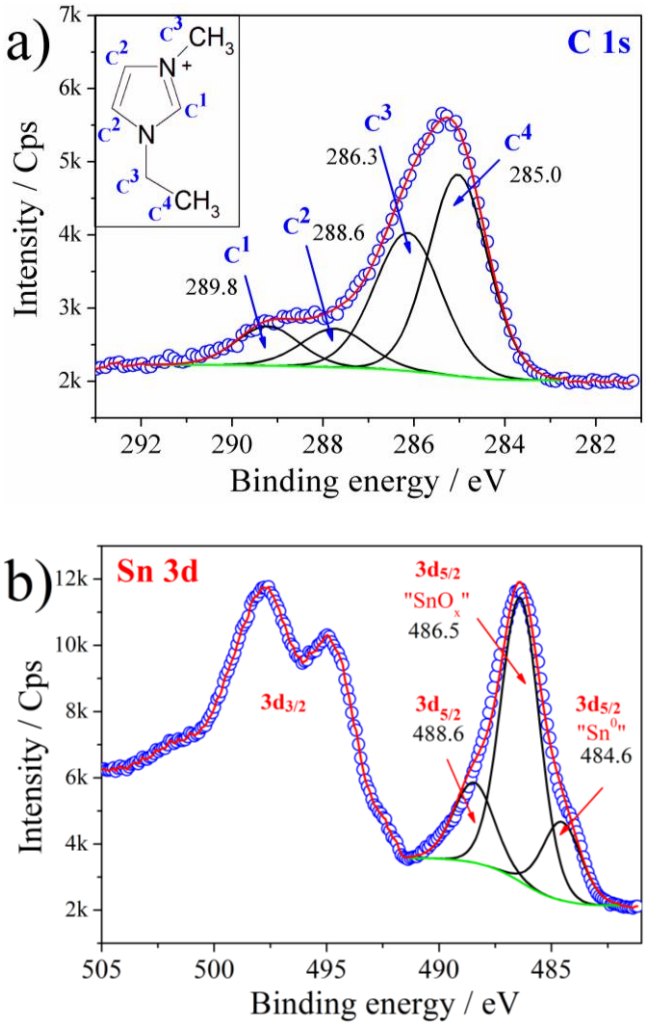

Figure 3. XPS spectra of C 1s (a), and Sn 3d (b) of Sn NPs synthesized in [$EMIm^+$][$TFSI^-$] washed with ACN + acetone.

After NPs washing with ACN and acetone, isolated NPs analyzed by PXRD (Figure 4) showed two well crystallized phases that are metallic β-Sn (space group $I4_1/amd$, ICSD 40037), and NaCl (space group Fm-3m, ICSD 165592), as secondary product of the reaction. The additional use of distilled water enabled to remove NaCl impurities leading to observed pattern of a single crystallized phase of metallic β-Sn without any evidence of crystalline oxidized SnO_x phases. Moreover, the effective removal of IL from the NPs surface was confirmed by thermogravimetric analysis (Figure S1 in Supporting Information).

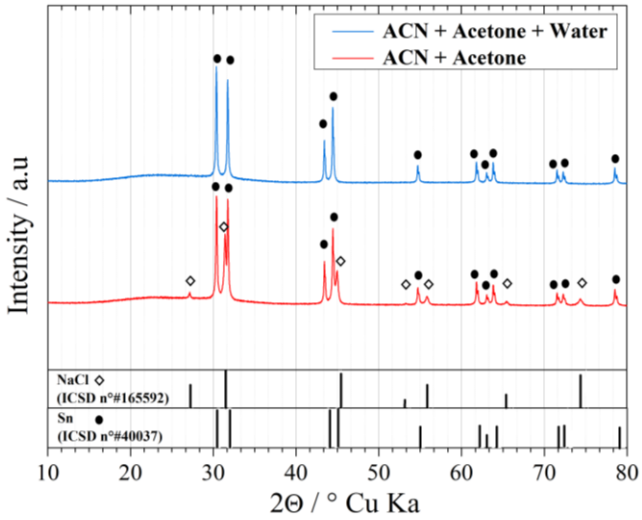

Figure 4. X-ray diffraction patterns of Sn NPs synthesized in [$EMIm^+$][$TFSI^-$] and washed with ACN + acetone firstly (red), followed by a washing step with distilled water (blue).

Transmission electron microscopy was used at different stages of the synthesis to study the evolution of the morphology of the NPs. Cryo-TEM (Figure 5.a) was used to characterize the NPs freshly prepared and still in the IL, *i.e.*, before isolation and washing steps. It showed dense packages of uniform NPs, all with spherical shape. Then after isolation, washing with ACN and acetone, as can be seen on Figure 5.b, the presence of nearly monodisperse particles with spherical

shape and a mean diameter (approximately 300 particles counted) of 10.9 ± 0.25 nm (Figure 5.b, inset) was observed. Finally, HRTEM (Figure 5.c) evidenced a core-shell structure of NPs, which was not observed on the NPs freshly, prepared and kept in the IL. The core of the nanoparticles was monocrystalline with interatomic planes distance of 0.29 nm assigned to the (002) plane of β-Sn phase. Moreover, the absence of interatomic planes of the shell indicated that it is amorphous. This result preliminary indicated that the shell consisted of oxidized phases as already observed by XPS, which was formed during the washing step. It should be noted that although the washing with distilled water did not affect the shape and the size of these NPs, the size of the shell seemed to slightly growth (see SI, Figure S2).

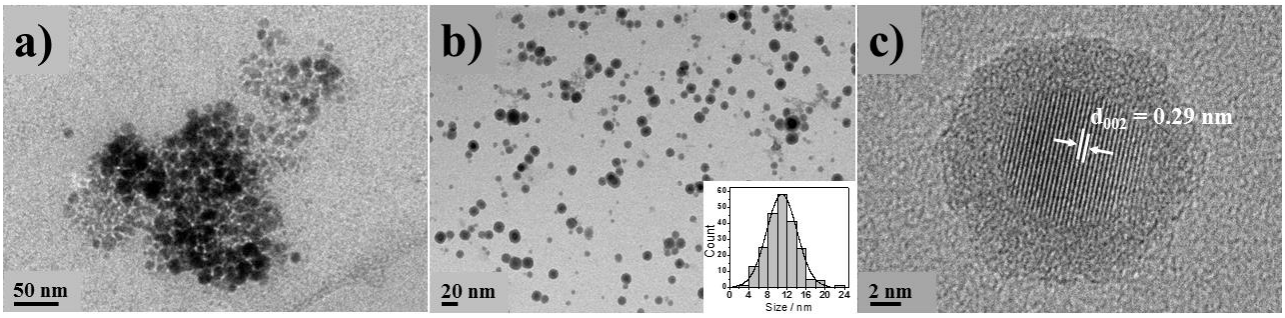

Figure 5. (a) Cryo-TEM image of Sn NPs synthesized in [$EMIm^+$][$TFSI^-$] frozen at 93 K, (b) TEM image of Sn NPs synthesized in [$EMIm^+$][$TFSI^-$] washed with ACN + acetone and histogram (inset) showing the particles size distribution, (c) HRTEM image of an isolated Sn NP after washing with ACN + acetone.

Characterizations of the core-shell NPs. Protesescu et al.[45] showed that solving the structure of core-shell structured Sn/SnO_x NPs was complex mostly due to the amorphous nature of the shell. They used up to three physical characterization tools including surface-enhanced NMR,

Mössbauer and X-ray absorption spectroscopies. Following their work, we used and confronted two complementary tools that are ^{119}Sn Mössbauer spectroscopy and the pair distribution function.

^{119}Sn Mössbauer spectroscopy is a powerful and sensitive tool for solids containing Sn, which allows to extract relevant information about the oxidation state and the local environment of tin.[46] Mössbauer spectra of Sn NPs were recorded first after the washing with ACN and acetone, and then after the ultimate washing with water in order to evaluate if an increase of oxidized phase's proportion had occured. The deconvolution of the Mössbauer spectra for the Sn NPs washed with acetonitrile and acetone (Figure 6.a), allowed to highlight three contributions corresponding to three different Sn oxidation states. These three subspectra might be associated with different Sn phases that could have different Debye temperatures (Θ_D) and thus different Lamb-Mössbauer factors (*f*), which were related to the subspectrum absorption area (*A*) through the equation (1) for $T > \Theta_D/2$:

$$\frac{d(\ln A)}{dT} = \frac{d(\ln f)}{dT} = \frac{-6E_R}{k\Theta_D^2} \qquad (1)$$

where E_R = 2.57 x 10^{-3} eV is the recoil energy of the γ-ray for ^{119}Sn and *k* the Boltzmann constant. Therefore, the evolution of each subspectrum area with temperature (See SI, Figure S3) allow us to estimate the Debye temperature (and the Lamb-Mössbauer factor) of the corresponding Sn phase (See SI, Table S1).

The refined Mössbauer hyperfine parameters (at 4.2 K) and the estimated Debye temperatures (See SI, Table S1) were consistent with crystalline β-Sn ($\Theta_D \approx 170$ K) for the Sn^0 quadrupole doublet with isomer shift δ = 2.63 mm.s^{-1} and low quadrupole splitting value,[46,47] amorphous SnO ($\Theta_D \approx 180$ K) for the Sn^{II} quadrupole doublet centered at δ = 2.94 mm.s^{-1} with a high value of quadrupole splitting (Δ ≈ 1.9 mm.s^{-1})[48] and amorphous SnO_2 ($\Theta_D \approx 240$ K) for the Sn^{IV} quadrupole doublet characterized by an isomer shift value close to zero (δ = 0.03 mm.s^{-1}).[46,49] All parameters

refined from Mössbauer data recorded at 4.2 K are listed in Table 1. Moreover, at 4.2 K the *f* factors were close to 1 then, the subspectra relative areas (Table 1) corresponded more accurately to the relative proportions of the three associated Sn phases. As it was presumed, Mössbauer spectroscopy showed, these Sn NPs presented a core of metallic tin (70%), and a shell that contained SnO (13%) and SnO_2 (17%) at the outer surface. Afterward, as expected NPs washed with water (Figure 6.b) exhibited a higher degree of oxidation, due to higher SnO and SnO_2 contents (16%, and 45%, respectively); accordingly a decrease of metallic Sn content at 39 % was observed.

These results correlate well with HRTEM and XPS data. Since the external oxide layer (with different oxidation states of Sn) formed on Sn NPs is very thin and did not exceed 10 nm, the oxidized SnO_x shell and the metallic Sn core of structure of NPs were detectable by XPS.[50]

Furthermore, Mössbauer analysis six weeks after were done on the same sample exposed to ambient atmosphere, and no increase of the oxide phases in detriment of metallic one was observed. The deconvolution of the spectra give quite identical proportions of the metallic Sn and SnO_x phases (see SI, Figure S4). The only small change observed was in the SnO/SnO_2 proportions (from 16% / 45% to 17% / 44%, respectively) determined at 4.2 K, and was not significant. (See SI, Table S2). Composition of the NPs after washing and exposure to ambient atmosphere is then rather stable. These results suggest that major oxidation occurred when NPs were in contact with water during the last washing step and point out that once the core-shell morphology was formed, it was stable even after long time exposure at ambient atmosphere.

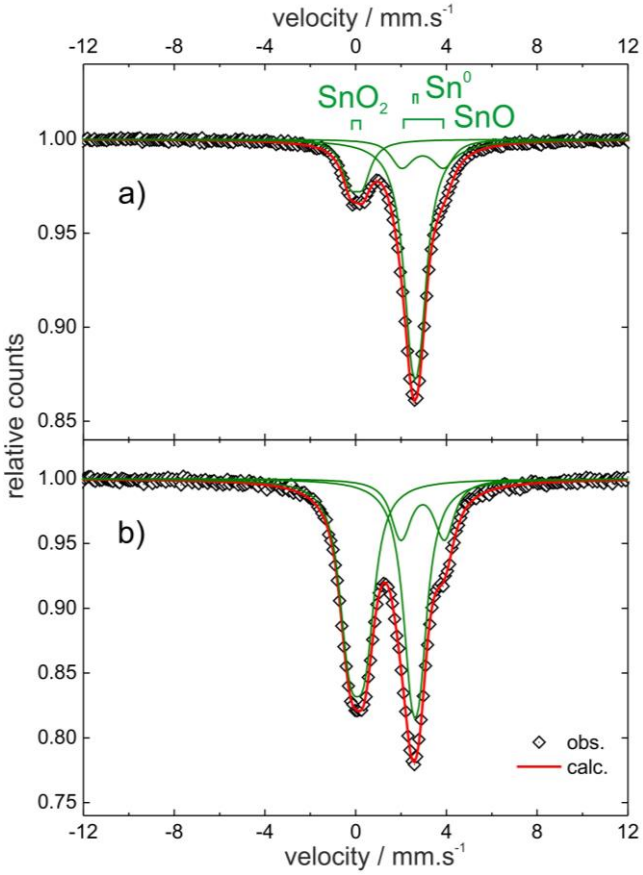

Figure 6. ^{119}Sn Mössbauer spectra recorded at 4.2 K of Sn NPs synthesized in [EMIm^{+}][TFSI^{-}] and washed with ACN + acetone (a), followed by a washing with water (b). Open circles represent raw data and solid lines represent the fitted spectra with three possible Sn species: β-Sn, SnO, and SnO_2, and open circles for raw data.

Table 1. ^{119}Sn Mössbauer hyperfine parameters (at 4.2 K) for Sn NPs synthesized in [$EMIm^+$][$TFSI^-$] (a) washed with ACN + acetone, (b) followed by a washing with water.

Samples			δ ($mm.s^{-1}$)	Δ ($mm.s^{-1}$)	Γ ($mm.s^{-1}$)	Area (%)
(a) ACN + Acetone	Sn	Sn^0	2.63(1)	0.31(2)	0.96(2)	70(2)
(4.2 K)	SnO	Sn^{II}	2.94(1)	1.88(2)	1.00(3)	13(2)
	SnO_2	Sn^{IV}	0.03(1)	0.52(2)	0.87(3)	17(2)
(b) ACN + Acetone + water	Sn	Sn^0	2.63(1)	0.35(2)	0.99(4)	39(2)
(4.2 K)	SnO	Sn^{II}	2.98(1)	1.90(2)	0.99(3)	16(2)
	SnO_2	Sn^{IV}	0.06(1)	0.65(1)	1.02(1)	45(2)

The PDF, G(r), is obtained by the Fourier transformation of total scattering data and is therefore perfectly suited with the characterization of amorphous/nanostructured materials such as the core-shell NPs. PDF, G(r), consists of a histogram of all interatomic distances in a sample. In this sense, an amorphous compound is characterized by atom-atom correlations with inter-atomic distances, denoted, *r*, that do not extend 10 Å. To investigate the PDF of the sample washed with water, *i.e.*, containing the largest content of amorphous oxide, we refined the PDF using the following procedure: (1) PDF data were refined over the intermediate/long *r*-range order where the amorphous signal was absent and the crystalline component predominant, *i.e.,* in the 8-35 Å *r*-range. Using a single phase of crystalline β-Sn phase (ICSD 40037), we obtained an excellent fit to the data with the weighted R-factor $R_{w1} \approx 6.5$ % (Figure 7.a). (2) The refinement was then performed on the 1 to 35 Å *r*-range, *i.e.*, including both the local and intermediate/long-range order and this led to an increase of the R_{w2} to 10.7 % with the residual curve pointing the presence of phases with no long-range order, *i.e.*, with correlations limited to 10 Å.[51] The inset in Figure 7.a. which represents the residual curve of PDF data at these low *r*-values, reflects the contribution

from additional phases, and shows in addition to peaks corresponding to metallic Sn (Sn^0−Sn^0 bond lengths, in pink), characteristic peaks corresponding to the Sn^{IV}−O, Sn^{IV}−Sn^{IV} bond lengths *i.e.*, SnO_2 as referred in the ICSD 9163 date file (blue) and Sn^{II} −O, Sn^{II} – Sn^{II} bond lengths, included in the data file of SnO *i.e.*, ICSD 15516 (in red). This suggested slight local distortion of metallic Sn in the core-shell architecture. (3) Subsequently, a three-phase refinement was performed (Figure 7.b) using Sn, SnO, and SnO_2, (ICSD 40037, 15516, and 9163 respectively) as structural models. The best fit (R_{w3} = 7.2 %) to the PDF data was achieved using an optimized spherical particle-size parameter of 9 Å for both SnO and SnO_2 phases, confirming their amorphous nature. These results are in agreement with Mössbauer and XPS data and confirmed that the shell was made of SnO_2 and SnO phases. Quantitative analysis yields atomic phase contents of 43 ± 4 % for Sn, 4 ± 3 % for SnO, and 53 ± 5 % for SnO_2. The proportion of Sn and amorphous SnO_x determined by Mössbauer and PDF analyses were comparable with 39 versus 43 % of Sn and 61 versus 57 % for the oxides phases, SnO_x, respectively. However, the relative % of SnO and SnO_2 phases was found quite different and this could be explained by the scaling of G(r) amplitude with the atomic mass number, *i.e.*, some peaks of O−O correlations being merely undetectable compared to Sn−Sn or Sn−O contributions. In our previous study,[26] the PDF refinement did not capture the presence of SnO_x because of its weaker content showing that the use of water effectively increased the proportion of oxidized phases. Moreover, it pointed the necessity to use complementary technique such as Mossbauer spectroscopy, to fully understand this complex architecture.

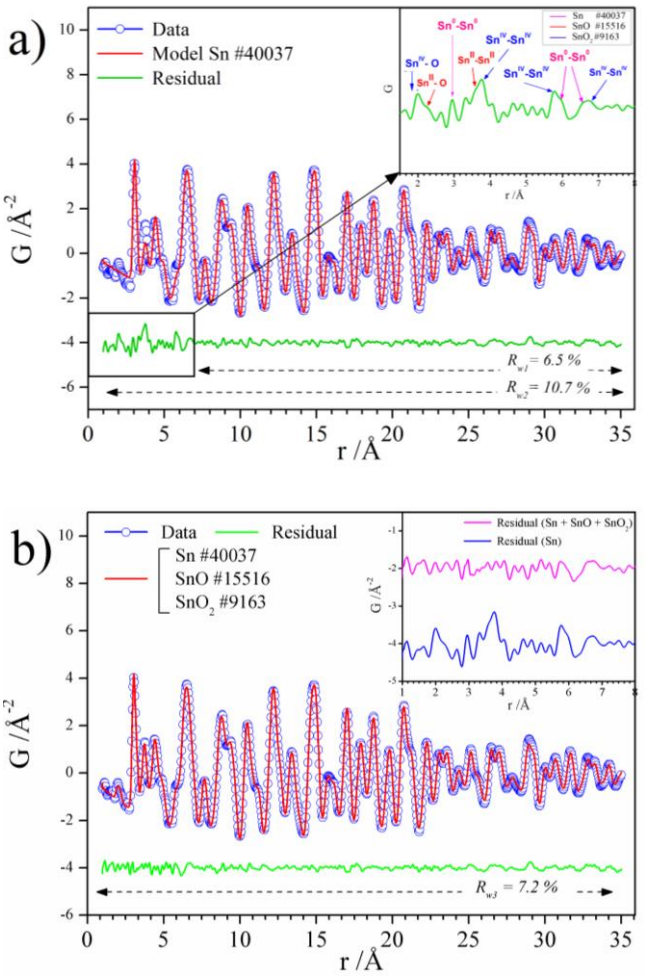

Figure 7. Experimental (blue curve) and calculated (red curve) pair distribution functions (PDF) obtained from high-energy X-ray scattering data for Sn NPs washed with ACN + acetone + water between 1 and 35 Å using as structural models (a) Sn and (b) Sn + SnO +SnO_2. The residual curve, difference between experimental data and calculated values is also shown (green curve).

The efficient removal of capping agents (and eventually secondary phase) of NPs is an important step for the fabrication of functionalized materials.[52] The reactivity of electrode materials toward oxidation is an important parameter as some electrode formulation uses aqueous based formulation such as aqueous based binders (e.g., carboxymethyl cellulose, poly(acrylic acid) or styrene butadiene rubber, …etc.).[52,53]

This work provided evidences about the oxidation sensibility of Sn-based NPs. It is known that bare metallic surface, due to their reactivity toward oxygen and water, are transformed in oxide. This is in fact one way to obtain oxidized surface of core/shell NPs or nanowires.[54-57] Note that once the core-shell morphology was formed, it was stable under long time exposure in ambient atmosphere. Hence, characterization of such architecture could be seen as a benchmark material to investigate how aforementioned and typical morphology affects the electrochemical properties which will be reported in a forthcoming study.

CONCLUSIONS.

In this work, Sn-based NPs with an average diameter of approximately 10 nm were synthesized at room temperature in an IL as reaction media. The morphology and structural features of the NPs were investigated using TEM and HRTEM images, showing a metallic β-Sn core consistent with PXRD analysis, and an amorphous shell composed of a first layer of SnO surrounded by a second layer of SnO_2, as evidenced by subsequent Mössbauer and PDF. The later analyses have allowed to acquire a better insight into the amorphous shell composition and to quantify each phase present in the sample. It highlighted that even in contact with traces of water, the amount of oxidized phase increase inevitably at the detriment of metallic Sn. Therefore, special attention must be paid during synthesis and isolation of NPs with drastic conditions avoiding any traces of water and oxygen if non oxidized Sn NPs have to be obtained. In addition, a washing method was successfully developed in order to remove IL and isolate NPs, leading to less than 1 % of IL. Imidazolium cation as residues of the IL were suggested by XPS, emphasizing a rather strong interaction between NPs and the cation of IL. The elaboration of a complete and multiple characterization procedure is an important preliminary groundwork to shed light on the structure-property relationships, essential to any understanding of electrochemical behavior especially in the case of

application as an electrode material for battery. Future work will be devoted to understand the impact of such Sn/SnO_x architecture on the electrochemical properties of this material.

AUTHOR INFORMATION

Corresponding Authors

*nadia.soulmi@upmc.fr, laurent.gaillon@upmc.fr

ACKNOWLEDGMENT

The authors gratefully thank Sandra Casale (LRS / UPMC-CNRS) for TEM and HRTEM observations, Jean-Michel Guigner (IMPMC / UPMC-CNRS-IRD-MNHN) for Cryo-TEM observations, and Delphine Talbot (PHENIX / UPMC-CNRS) for TGA-DTA analysis.

REFERENCES

(1) Yasuyuki, M.; Kunihiro, K.; Kurissery, S.; Kanavillil, N.; Sato, Y.; Kikuchi, Y. Antibacterial Properties of Nine Pure Metals: A Laboratory Study Using *Staphylococcus Aureus* and *Escherichia Coli*. *Biofouling* **2010**, *26* (7), 851–858

(2) Song, J.; Wang, L.; Zibart, A.; Koch, C. Corrosion Protection of Electrically Conductive Surfaces. *Metals* **2012**, *2* (4), 450–477.

(3) Nayral, C.; Viala, E.; Fau, P.; Senocq, F.; Jumas, J.-C.; Maisonnat, A.; Chaudret, B. Synthesis of Tin and Tin Oxide Nanoparticles of Low Size Dispersity for Application in Gas Sensing. *Methods* **2000**, *4082*, 4090.

(4) Bhattacharjee, A.; Ahmaruzzaman, M. Photocatalytic-Degradation and Reduction of Organic Compounds Using SnO_2 Quantum Dots (via a Green Route) under Direct Sunlight. *RSC Adv.* **2015**, *5* (81), 66122–66133.

(5) Hermans, S.; Raja, R.; Thomas, J. M.; Johnson, B. F.; Sankar, G.; Gleeson, D. Solvent-Free, Low-Temperature, Selective Hydrogenation of Polyenes Using a Bimetallic Nanoparticle Ru–Sn Catalyst. *Angew. Chem. Int. Ed.* **2001**, *40* (7), 1211–1215.

(6) Bazin, L.; Mitra, S.; Taberna, P. L.; Poizot, P.; Gressier, M.; Menu, M. J.; Barnabé, A.; Simon, P.; Tarascon, J.-M. High Rate Capability Pure Sn-Based Nano-Architectured Electrode Assembly for Rechargeable Lithium Batteries. *J. Power Sources* **2009**, *188* (2), 578–582.

(7) Hassoun, J.; Fernicola, A.; Navarra, M. A.; Panero, S.; Scrosati, B. An Advanced Lithium-Ion Battery Based on a Nanostructured Sn–C Anode and an Electrochemically Stable LiTFSi-Py_{24}TFSI Ionic Liquid Electrolyte. *J. Power Sources* **2010**, *195* (2), 574–579.

(8) Naille, S.; Ionica-Bousquet, C. M.; Robert, F.; Morato, F.; Lippens, P.-E.; Olivier-Fourcade, J. Sn-Based Intermetallic Materials: Performances and Mechanisms. *J. Power Sources* **2007**, *174* (2), 1091–1094.

(9) Groult, H.; El Ghallali, H.; Barhoun, A.; Briot, E.; Julien, C. M.; Lantelme, F.; Borensztjan, S. Study of Co–Sn and Ni–Sn Alloys Prepared in Molten Chlorides and Used as Negative Electrode in Rechargeable Lithium Battery. *Electrochimica Acta* **2011**, *56* (6), 2656–2664.

(10) Winter, M.; Besenhard, J. O. Electrochemical Lithiation of Tin and Tin-Based Intermetallics and Composites. *Electrochimica Acta* **1999**, *45* (1), 31–50.

(11) Bresser, D.; Mueller, F.; Buchholz, D.; Paillard, E.; Passerini, S. Embedding Tin Nanoparticles in Micron-Sized Disordered Carbon for Lithium-and Sodium-Ion Anodes. *Electrochimica Acta* **2014**, *128*, 163–171.

(12) Mukherjee, R.; Krishnan, R.; Lu, T.-M.; Koratkar, N. Nanostructured Electrodes for High-Power Lithium Ion Batteries. *Nano Energy* **2012**, *1* (4), 518–533.

(13) Aricò, A. S.; Bruce, P.; Scrosati, B.; Tarascon, J.-M.; Van Schalkwijk, W. Nanostructured Materials for Advanced Energy Conversion and Storage Devices. *Nat. Mater.* **2005**, *4* (5), 366–377.

(14) Peng, Z.; Yang, H. Designer Platinum Nanoparticles: Control of Shape, Composition in Alloy, Nanostructure and Electrocatalytic Property. *Nano Today* **2009**, *4* (2), 143–164.

(15) Wang, X.; Zhuang, J.; Peng, Q.; Li, Y. A General Strategy for Nanocrystal Synthesis. *Nature* **2005**, *437* (7055), 121–124.

(16) Wang, Y.; Xia, Y. Bottom-up and Top-down Approaches to the Synthesis of Monodispersed Spherical Colloids of Low Melting-Point Metals. *Nano Lett.* **2004**, *4* (10), 2047–2050.

(17) Mallikarjuna, N. N.; Varma, R. S. Microwave-Assisted Shape-Controlled Bulk Synthesis of Noble Nanocrystals and Their Catalytic Properties. *Cryst. Growth Des.* **2007**, *7* (4), 686–690.

(18) Jana, N. R.; Gearheart, L.; Murphy, C. J. Seed-Mediated Growth Approach for Shape-Controlled Synthesis of Spheroidal and Rod-like Gold Nanoparticles Using a Surfactant Template. *Adv. Mater.* **2001**, *13* (18), 1389.

(19) Niu, Z.; Li, Y. Removal and Utilization of Capping Agents in Nanocatalysis. *Chem. Mater.* **2013**, *26* (1), 72–83.

(20) Becker, M. D.; Wang, Y.; Pennell, K. D.; Abriola, L. M. A Multi-Constituent Site Blocking Model for Nanoparticle and Stabilizing Agent Transport in Porous Media. *Environ. Sci. Nano* **2015**, *2* (2), 155–166.

(21) Welton, T. Room-Temperature Ionic Liquids. Solvents for Synthesis and Catalysis. *Chem. Rev.* **1999**, *99* (8), 2071–2084.

(22) Antonietti, M.; Kuang, D.; Smarsly, B.; Zhou, Y. Ionic Liquids for the Convenient Synthesis of Functional Nanoparticles and Other Inorganic Nanostructures. *Angew. Chem. Int. Ed.* **2004**, *43* (38), 4988–4992.

(23) Ueno, K.; Watanabe, M. From Colloidal Stability in Ionic Liquids to Advanced Soft Materials Using Unique Media. *Langmuir* **2011**, *27* (15), 9105–9115.

(24) Migowski, P.; Machado, G.; Texeira, S. R.; Alves, M. C.; Morais, J.; Traverse, A.; Dupont, J. Synthesis and Characterization of Nickel Nanoparticles Dispersed in Imidazolium Ionic Liquids. *Phys. Chem. Chem. Phys.* **2007**, *9* (34), 4814–4821.

(25) Redel, E.; Thomann, R.; Janiak, C. First Correlation of Nanoparticle Size-Dependent Formation with the Ionic Liquid Anion Molecular Volume. *Inorg. Chem.* **2008**, *47* (1), 14–16.

(26) Le Vot, S.; Dambournet, D.; Groult, H.; Ngo, A.; Petit, C.; Rizzi, C.; Salzemann, C.; Sirieix-Plenet, J.; Borkiewicz, O. J.; Raymundo-Piñero, E.; Gaillon, L. Synthesis of Tin Nanocrystals in Room Temperature Ionic Liquids. *Dalton Trans.* **2014**, *43* (48), 18025–18034.

(27) He, Z.; Alexandridis, P. Nanoparticles in Ionic Liquids: Interactions and Organization. *Phys. Chem. Chem. Phys.* **2015**, *17* (28), 18238–18261.

(28) Canongia Lopes, J. N.; Padua, A. A. Nanostructural Organization in Ionic Liquids. *J. Phys. Chem. B* **2006**, *110* (7), 3330–3335.

(29) Ayi, A. A.; Khare, V.; Strauch, P.; Girard, J.; Fromm, K. M.; Taubert, A. On the Chemical Synthesis of Titanium Nanoparticles from Ionic Liquids. *Monatshefte Für Chem.-Chem. Mon.* **2010**, *141* (12), 1273–1278.

(30) Brand, R. A. WinNormos Mössbauer Fitting Program. *Univ. Duisburg* **2008**.

(31) Qiu, X.; Thompson, J. W.; Billinge, S. J. PDFgetX2: A GUI-Driven Program to Obtain the Pair Distribution Function from X-Ray Powder Diffraction Data. *J. Appl. Crystallogr.* **2004**, *37* (4), 678–678.

(32) Chaudhuri, S.; Chupas, P.; Morgan, B. J.; Madden, P. A.; Grey, C. P. An Atomistic MD Simulation and Pair-Distribution-Function Study of Disorder and Reactivity of α-AlF_3 Nanoparticles. *Phys. Chem. Chem. Phys.* **2006**, *8* (43), 5045–5055.

(33) Inorganic Crystal Structure Database. http://icsd.fiz-karlsruhe.de/icsd (Accessed Jan 23, 2017).

(34) Dambournet, D.; Duttine, M.; Chapman, K. W.; Wattiaux, A.; Borkiewicz, O.; Chupas, P. J.; Demourgues, A.; Groult, H. Resolving and Quantifying Nanoscaled Phases in Amorphous FeF_3 by Pair Distribution Function and Mössbauer Spectroscopy. *J. Phys. Chem. C* **2014**, *118* (25), 14039–14043.

(35) Recham, N.; Dupont, L.; Courty, M.; Djellab, K.; Larcher, D.; Armand, M.; Tarascon, J.-M. Ionothermal Synthesis of Tailor-Made $LiFePO_4$ Powders for Li-Ion Battery Applications. *Chem. Mater.* **2009**, *21* (6), 1096–1107.

(36) Sarraute, S.; Costa Gomes, M. F.; Pádua, A. A. Diffusion Coefficients of 1-Alkyl-3-Methylimidazolium Ionic Liquids in Water, Methanol, and Acetonitrile at Infinite Dilution. *J. Chem. Eng. Data* **2009**, *54* (9), 2389–2394.

(37) Wagner, C. D.; Muilenberg, G. E. *Handbook of X-Ray Photoelectron Spectroscopy*; Perkin-Elmer, 1979.

(38) Seo, S.; Park, J.; Kang, Y.-C. Chemical Analysis of Ionic Liquids Using Photoelectron Spectroscopy. *Bull. Korean Chem. Soc.* **2016**, *37* (3), 355–360.

(39) Neouze, M.-A. About the Interactions between Nanoparticles and Imidazolium Moieties: Emergence of Original Hybrid Materials. *J. Mater. Chem.* **2010**, *20* (43), 9593–9607.

(40) Schrekker, H. S.; Gelesky, M. A.; Stracke, M. P.; Schrekker, C. M.; Machado, G.; Teixeira, S. R.; Rubim, J. C.; Dupont, J. Disclosure of the Imidazolium Cation Coordination and Stabilization Mode in Ionic Liquid Stabilized Gold (0) Nanoparticles. *J. Colloid Interface Sci.* **2007**, *316* (1), 189–195.

(41) Zhang, H.; Cui, H. Synthesis and Characterization of Functionalized Ionic Liquid-Stabilized Metal (Gold and Platinum) Nanoparticles and Metal Nanoparticle/Carbon Nanotube Hybrids. *Langmuir* **2009**, *25* (5), 2604–2612.

(42) Li, J.-T.; Świątowska, J.; Maurice, V.; Seyeux, A.; Huang, L.; Sun, S.-G.; Marcus, P. XPS and ToF-SIMS Study of Electrode Processes on Sn−Ni Alloy Anodes for Li-Ion Batteries. *J. Phys. Chem. C* **2011**, *115* (14), 7012–7018.

(43) Świątowska-Mrowiecka, J.; Maurice, V.; Zanna, S.; Klein, L.; Marcus, P. XPS Study of Li Ion Intercalation in V_2O_5 Thin Films Prepared by Thermal Oxidation of Vanadium Metal. *Electrochimica Acta* **2007**, *52* (18), 5644–5653.

(44) Naille, S.; Dedryvère, R.; Martinez, H.; Leroy, S.; Lippens, P. E.; Jumas, J.-C.; Gonbeau, D. XPS Study of Electrode/Electrolyte Interfaces of Eta-Cu_6Sn_5 Electrodes in Li-Ion Batteries. *J. Power Sources* **2007**, *174*, 1086–1090.

(45) Protesescu, L.; Rossini, A. J.; Kriegner, D.; Valla, M.; De Kergommeaux, A.; Walter, M.; Kravchyk, K. V.; Nachtegaal, M.; Stangl, J.; Malaman, B.; Reiss, P.; Lesage, A.; Emsley,

L.; Copéret, C.; Kovalenko, M.V. Unraveling the Core–Shell Structure of Ligand-Capped Sn/SnO_x Nanoparticles by Surface-Enhanced Nuclear Magnetic Resonance, Mössbauer, and X-Ray Absorption Spectroscopies. *ACS Nano* **2014**, *8* (3), 2639–2648.

(46) Moreno, M. S.; Mercader, R. C.; Bibiloni, A. G. Study of Intermediate Oxides in SnO Thermal Decomposition. *J. Phys. Condens. Matter* **1992**, *4* (2), 351.

(47) Hightower, A.; Delcroix, P.; Le Caër, G.; Huang, C.-K.; Ratnakumar, B. V.; Ahn, C. C.; Fultz, B. A ^{119}Sn Mössbauer Spectrometry Study of Li-SnO Anode Materials for Li-Ion Cells. *J. Electrochem. Soc.* **2000**, *147* (1), 1–8.

(48) Williams, K. F. E.; Johnson, C. E.; Johnson, J. A.; Holland, D.; Karim, M. M. Mossbauer Spectra of Tin in Binary Si-Sn Oxide Glasses. *J. Phys. Condens. Matter* **1995**, *7* (49), 9485.

(49) Sougrati, M. T.; Jouen, S.; Hannoyer, B. Relative Lamb–Mössbauer Factors of Tin Corrosion Products. *Hyperfine Interact.* **2006**, *167* (1–3), 815–818.

(50) Lu, F.; Ji, X.; Yang, Y.; Denga, W.; Banks, C. E. Room temperature ionic liquid assisted well-dispersed core-shell tin nanoparticles through cathodic corrosion. *RSC Adv*. **2013**, *3*, 18791–18793

(51) Dambournet, D.; Chapman, K. W.; Chupas, P. J.; Gerald, R. E.; Penin, N.; Labrugere, C.; Demourgues, A.; Tressaud, A.; Amine, K. Dual Lithium Insertion and Conversion Mechanisms in a Titanium-Based Mixed-Anion Nanocomposite. *J. Am. Chem. Soc.* **2011**, *133* (34), 13240–13243.

(52) Li, J.; Le, D.-B.; Ferguson, P. P.; Dahn, J. R. Lithium Polyacrylate as a Binder for Tin–cobalt–carbon Negative Electrodes in Lithium-Ion Batteries. *Electrochimica Acta* **2010**, *55* (8), 2991–2995.

(53) Zhang, W.; Dahbi, M.; Komaba, S. Polymer Binder: A Key Component in Negative Electrodes for High-Energy Na-Ion Batteries. *Curr. Opin. Chem. Eng.* **2016**, *13*, 36–44.

(54) Kumar, N.; Auffan, M.; Gattacceca, J.; Rose, J.; Olivi, L.; Borschneck, D.; Kvapil, P.; Jublot, M.; Kaifas, D.; Malleret, L.; Doumenq, P.; Bottero, J.-Y. Molecular Insights of Oxidation Process of Iron Nanoparticles: Spectroscopic, Magnetic, and Microscopic Evidence. *Environ. Sci. Technol.* **2014**, *48*, 13888-13894.

(55) Kolmakov, A.; Zhang, Y.; Moskovits, M. Topotactic Thermal Oxidation of Sn Nanowires: Intermediate suboxides and core-shell Metastable Structures *Nano Lett.*, **2003**, *3* (8), 1125-1129.

(56) Fujihara, S.; Maeda, T.; Ohgi, H.; Hosono, E.; Imai, H.; Kim, S.-H. Hydrothermal Routes To Prepare Nanocrystalline Mesoporous SnO_2 Having High Thermal Stability. *Langmui*r **2004**, 20, 6476-6481.

(57) Jagminas, A.; Morales, F. M.; Mazeika, K. ;Veronese, G. P. ; Reklaitis, J. ;Lozano, J. G. ; Manuel, J. M. ; Garcia, R. ; Kurtinaitiene, M.; Juskenas, R.; Baltrunas, D. Fabrication of Barbed-Shaped SnO@SnO_2 Core/Shell Nanowires, *J. Phys. Chem. C* **2011**, 115, 4495-4501.

FOR TABLE OF CONTENTS ONLY.

TABLE OF CONTENTS SYNOPSIS. The structure of monodisperse Sn/SnO_x core-shell nanoparticles initially synthesized in ionic liquid and isolated from it was resolved using multiple characterization methods, yielding to a crystalline and metallic Sn core and an amorphous shell composed of a first ultra-thin layer of SnO under a second layer of SnO_2. The quantification of each phase during the washing procedure highlighted the protective role of ionic liquid against oxidation, additionally to it stabilizing properties to generate small nanoparticles.

TABLE OF CONTENTS GRAPHIC.

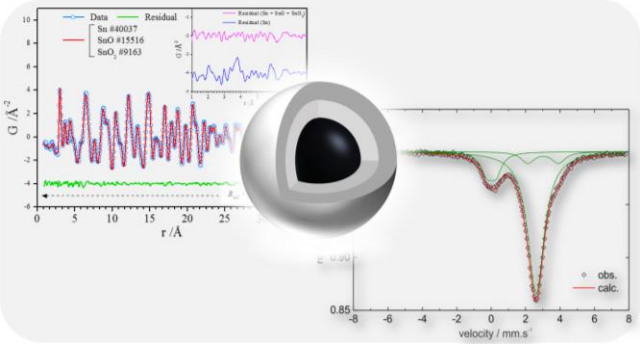

Structural and morphological description of Sn/SnO_x core-shell nanoparticles synthesized and isolated from ionic liquid

Nadia Soulmi [a,], Damien Dambournet [a], Cécile Rizzi [a], Juliette Sirieix-Plénet [a], Mathieu Duttine [b], Alain Wattiaux [b], Jolanta Swiatowska [c], Olaf J. Borkiewicz [d], Henri Groult [a], and Laurent Gaillon [a,*]*

[a] Sorbonne Universités, UPMC Univ Paris 06, CNRS, Laboratoire PHENIX, F-75005 Paris, France

[b] CNRS, Université de Bordeaux, ICMCB, UPR 9048, F-33600 Pessac, France

[c] PSL Research University, Chimie ParisTech - CNRS, Institut de Recherche de Chimie Paris, F-75005 Paris, France

[d] X-ray Science Division, Advanced Photon Source, Argonne National Laboratory, Argonne, Illinois 60439, United States

SUPPORTING INFORMATION

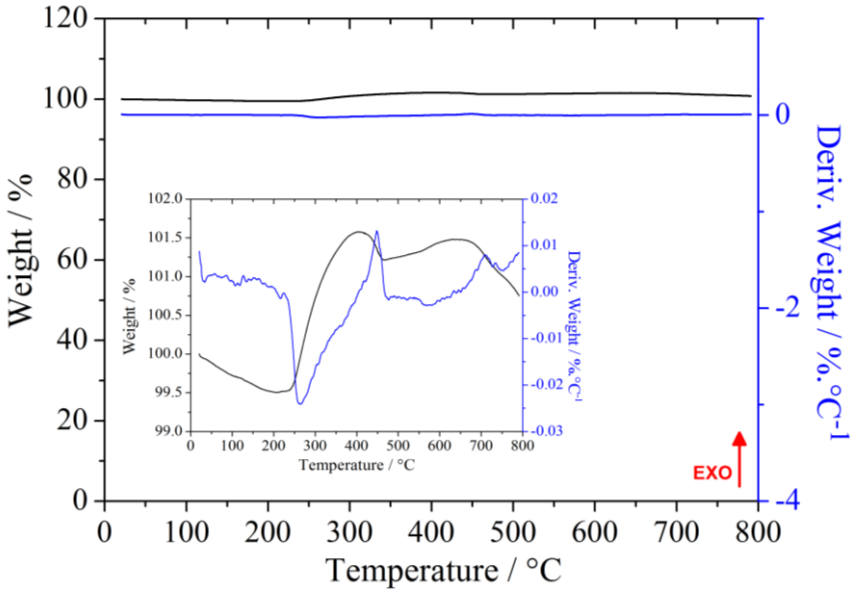

Figure S1. TGA analysis of Sn NPs synthesized in [EMIm$^+$][TFSI$^-$] after washing with ACN + acetone + water (black line), with the corresponding derivative curve of the weight loss to temperature (blue line). Zoom in 99 to 102 % weight range (inset).

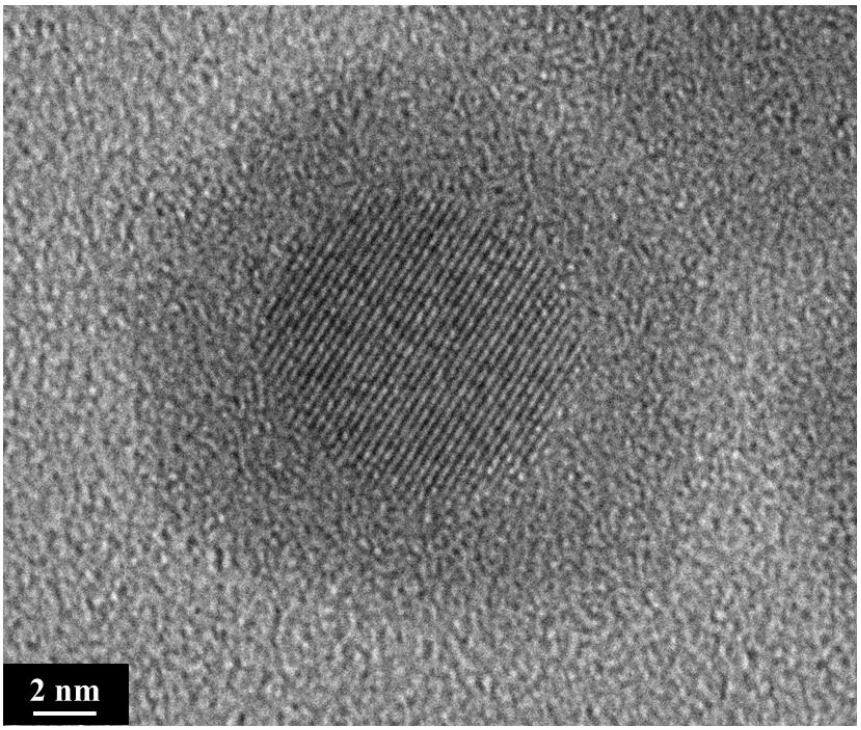

Figure S2. HRTEM images of Sn NPs synthesized in [EMIm$^+$][TFSI$^-$] washed with ACN + acetone + water.

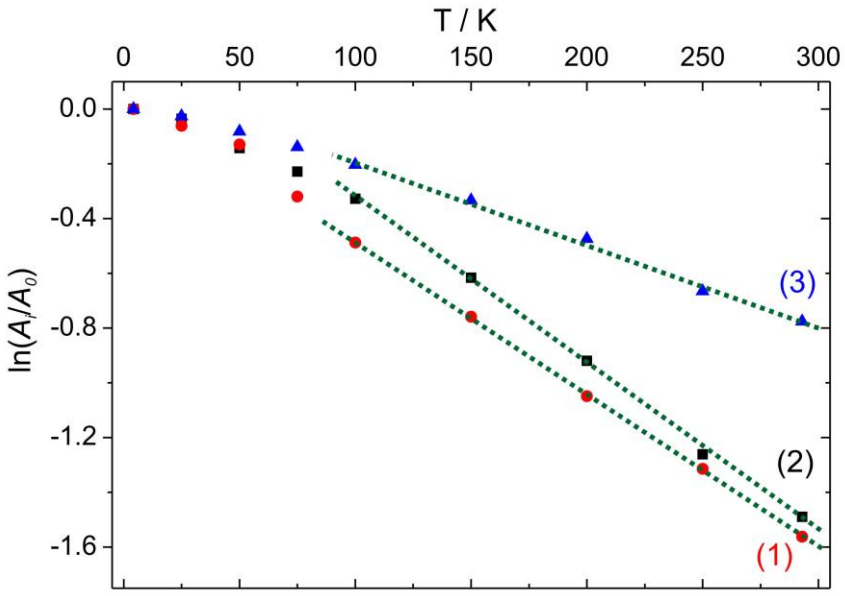

Figure S3. Temperature dependence of the natural logarithm of the normalized area A/A_i of the Mössbauer subspectra attributed to (1) β-Sn, (2) SnO and (3) SnO_2 phases for Sn NPs synthesized in [$EMIm^+$][$TFSI^-$] and washed with ACN + acetone. The dashed lines represent the linear fits of data for T > 100 K with $\Theta_D(1)$ = 171 K, $\Theta_D(2)$ = 179 K and $\Theta_D(3)$ = 242 K.

Table S1. Debye temperature (Θ_D) and Lamb-Mössbauer factor (f) at room temperature extracted from the analysis of the Sn NPs (synthesized in [$EMIm^+$][$TFSI^-$] and washed with ACN + acetone) Mössbauer spectra recorded from room temperature down to 4.2 K.

Signal	Assignment	Θ_D (K)	f at 293 K
(1)	β-Sn	171(2)	0.17
(2)	SnO	179(3)	0.20
(3)	SnO_2	242(3)	0.41

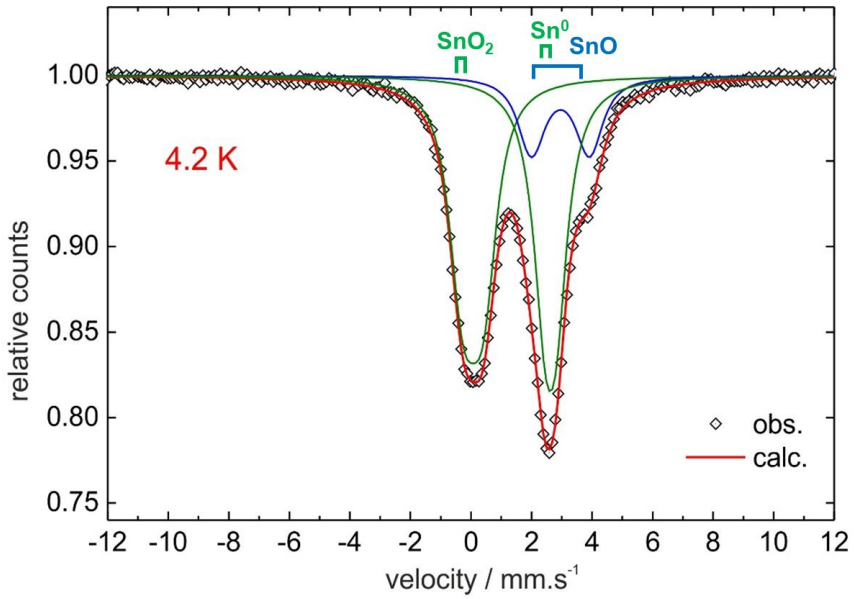

Figure S4. ^{119}Sn Mössbauer spectra recorded at 4.2 K of Sn NPs synthesized in [EMIm$^+$][TFSI$^-$] and washed with ACN + acetone + water, six weeks after exposure under ambient atmosphere. Open circles represent raw data and solid lines represent the fitted spectra with three possible Sn species: β-Sn, SnO, and SnO_2.

Table S2. ^{119}Sn Mössbauer hyperfine parameters (at 4.2 K) for Sn NPs synthesized in [EMIm$^+$][TFSI$^-$] washed with ACN + acetone + water, six weeks after exposure under ambient atmosphere.

Samples 6 weeks after			δ (mm.s^{-1})	Δ (mm.s^{-1})	Γ (mm.s^{-1})	Area (%)
ACN + Acetone + water (4.2 K)	**Sn**	Sn^0	2.625(3)	0.37(2)	0.95(3)	39(2)
	SnO	Sn^{II}	2.955(8)	1.90(3)	0.95(3)	17(2)
	SnO_2	Sn^{IV}	0.066(2)	0.67(1)	0.90(2)	44(2)